ARTICLE

Check for updates

Dispersive and dissipative coupling of photon Bose-Einstein condensates

Chris Toebes [1], Mario Vretenar[1] & Jan Klaers [1]✉

The synchronization of coherent states of light has long been an important subject of basic research and technology. Recently, a new concept for analog computers has emerged where this synchronization process can be exploited to solve computationally hard problems - potentially faster and more energy-efficient than what can be achieved with conventional computer technology today. The unit cell of such systems consists of two coherent centers that are coupled to one another in a controlled manner. Here, we experimentally characterize and analyze the synchronization process of two photon Bose-Einstein condensates, which are coupled to one another, either dispersively or dissipatively. We show that both types of coupling are robust against a detuning of the condensate frequencies and show similar time constants in establishing mutual coherence. Significant differences between these couplings arise in the behaviour of the condensate populations under imbalanced optical pumping. The combination of these two types of coupling extends the class of physical models that can be investigated using analog simulations.

[1] Adaptive Quantum Optics (AQO), MESA+ Institute for Nanotechnology, University of Twente, PO Box 217, 7500 AE Enschede, The Netherlands.
✉email: j.klaers@utwente.nl

Analog simulations are of great importance in physics whenever a physical problem cannot be solved exactly or numerically due to its mathematical complexity. In recent years, such simulations have gained attention as a possible method to outperform the current standard of digital silicon computers in specific computational tasks. Of particular interest in this regard is optical spin-glass simulation[1–18]. Here, a system of coupled coherent states of light is used to simulate classical spin models such as the Ising[19] or XY model[20,21]. The basic idea behind these simulators is to map the Hamiltonian of a classical spin model to the gain function of an optical system. A mode competition is then set in motion by optical pumping, which leads to a sampling of low-energy configurations of the simulated spin model. This can provide, for example, interesting insight into physics of magnetic systems, such as the Berezinskii-Kosterlitz-Thouless (BKT) transition[20,21]. However, the potential applications of such simulators go far beyond physics, since finding the lowest energy configuration of a spin model with sufficiently general couplings (spin-glass problem) is known to be a NP-hard optimization problem[22,23]. A device that can produce solutions to the spin-glass problem quickly and energy-efficiently will also be highly useful for providing solutions to mathematically equivalent optimization tasks that are ubiquitous in modern society, like job scheduling and the knapsack problem[24]. For the Ising model, a first generation of analog spin-glass simulators has been realized using networks of superconducting qubits[25,26] and optical parametrical oscillators[2–5]. For the XY model, the proposed physical platforms are based on superconducting qubits[27], lasers[1,12–14,28,29], atomic Bose-Einstein condensates (BEC)[30], and optical BECs[6–8,10,11,15,16,31,32].

An optical XY spin-glass simulator consists of a lattice of coherent states of light, which represent the XY spins, i.e., angular degrees of freedom $\theta_i \in [0, 2\pi)$ in the simulated model. By physically coupling these states, one tries to map the Hamiltonian of the simulated XY model, i.e., $H_{XY} = -\Sigma J_{ij} \cos(\theta_i - \theta_j)$, to the gain function of the simulator system. It is important to distinguish the physical couplings in the simulator system from the coupling constants in the simulated model. While the couplings in the simulated XY model are real-valued ($J_{ij} \in \mathbb{R}$), the physical couplings between the coherent states in the simulator system are generally described by complex-valued parameters since the simulators typically operate under non-equilibrium conditions, i.e., they are determined by gain and loss. The coupling in these simulator systems is typically divided into two groups, namely dispersive and dissipative[33,34]. Dispersive coupling is caused by direct particle exchange between the coherent centers. Here, the coupling constant is real-valued and in turn leads to splitting in the eigenfrequencies of the coupled system. In contrast, dissipative coupling is caused by the state of one coherent center

affecting the loss rate of another and therefore has an imaginary coupling constant. This leads to a splitting in the imaginary component of the eigenfrequencies of the coupled system.

The nature of the couplings between the coherent centers dictates the overall dynamics of the simulator system. The couplings not only define a specific gain function but also determine whether the system is aiming for fixed points in the configuration space. Investigating the fundamental differences between dispersive and dissipative coupling is therefore critical to understanding and improving optical spin-glass simulators and is the basis for extending their simulation capabilities to a larger class of physical models. In this work, we investigate a system of two coupled photon BECs[35–43], in which the flow of the photons is controlled in such a way that either a predominantly dispersive or a dissipative coupling of the condensates is created. We find similar coupling strengths of several 10 GHz for both types of coupling. A time-resolved measurement reveals the fast dynamics in these systems, e.g., condensation and the establishment of coherence within several 100 ps. A fundamental difference in the physical behavior of the two types of coupling arises in the case of unbalanced optical pumping.

Results

Our experimental setup consists of a high-finesse optical microcavity filled with rhodamine 6G dissolved in ethylene glycol as optically active medium, see Fig. 1a. One of the cavity mirrors is fixed in position, while the other is controlled by three piezo actuators that allow for precise adjustment of the cavity length and tilt. The frequency-dependent absorption and emission coefficients of the dye follow the Kennard-Stepanov law: $B_{12}(\omega)/B_{21}(\omega) = \exp[\hbar(\omega - \omega_{zpl})/kT]$, where ω_{zpl} is the zero-phonon line of the dye. This means that the absorption $B_{12}(\omega)$ and emission $B_{21}(\omega)$ are related by a Boltzmann factor. The high-reflectivity mirrors confine the photons and allow for repeated absorption and re-emission by the dye molecules before leaving the cavity. This brings the photon gas in thermal equilibrium with the dye and allows for the formation of a BEC at room temperature[35,36]. When the separation between the microcavity mirrors is sufficiently small, the free spectral range can become comparable to the emission bandwidth of the dye. This leads to a conservation of the longitudinal mode number of the photons when interacting with the optical medium, which effectively makes the photon gas two-dimensional. The energy of a photon can then be approximated by

$$E \simeq \frac{mc^2}{n_0^2} + \frac{(\hbar k_r)^2}{2m} - \frac{mc^2}{n_0^2}\frac{\Delta d}{D_0},\tag{1}$$

where m denotes the effective photon mass, n_0 is refractive index of the dye medium, k_r is the transversal wavenumber, D_0 is the
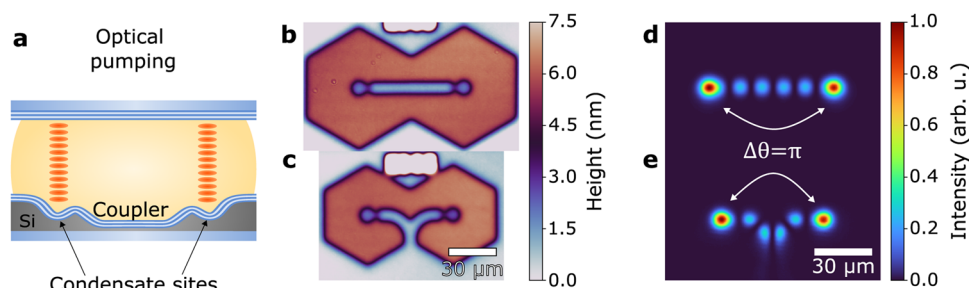

Fig. 1 Overview of the experiment and investigated coupling structures. a Schematic representation (cross section) of the microcavity. The cavity consists of two highly reflective mirrors and is filled with a rhodamine 6G dye solution. A nanostructured mirror creates two circular confining potential, where photon BECs form after local excitation with an optical pump beam. The coupling is determined by the potential landscape between the condensates. **b, c** Height map of the structure for the direct and Y-coupling potential, respectively. **d, e** Measured photon densities under symmetric excitation for the direct coupler and the Y-coupler, respectively. These images are acquired by imaging the light that leaves the microcavity onto a camera.

mean mirror separation and Δd is a (small) change in mirror separation over the surface. The first term corresponds to the rest energy of the photon, the second term corresponds to the kinetic energy and the final term is equivalent to the potential energy. In this experiment we use two methods for controlling the potential energy term. The first is a nanostructuring technique based on direct-laser writing that generates a well defined height profile on the mirror[44]. The second is precise adjustment of the tilt angle between the two cavity mirrors by piezo-electric actuation. The tilt translates into a height (hence potential) gradient in the cavity.

Dispersive and dissipative coupling. The nanostructured mirrors that are used to create and investigate dispersive and dissipative couplings between two photon BECs are shown in Fig. 1b and c. For the sake of simplicity, we refer to these structures as direct coupling and Y-coupling structure. The direct coupler (Fig. 1b) has been introduced in our previous work and can be considered as a photonic Josephson junction[18]. It realizes (predominantly) dispersive coupling between condensates. Its height profile creates two circular confining potentials that can host localized photon BECs. Optically pumping these sites induces a high local chemical potential, leading to the formation of a photon BEC. The condensate locations are connected by a waveguiding potential at a lower potential energy. Photons that leak from one of the condensates gain kinetic energy as they enter this waveguiding potential and form a traveling wave towards the other condensate. The phase difference that the light accumulates while traveling through the waveguide determines whether the condensates couple in phase or in antiphase. Figure 1d shows an example of the photon density inside the microcavity plane obtained by observing the light that is transmitted through one of the cavity mirrors. The shown density pattern indicates an antisymmetric wavefunction that corresponds to an antiphase coupling of the two condensates. In order to achieve a dissipative coupling, a direct exchange of particles between the condensates should be avoided. Instead, we propose to use a potential landscape that realizes a Y-coupling between the condensates. This structure defines a loss channel for the coupled condensate system, i.e., the open end of the Y-coupling, which depends on the relative phase of the two condensates: if the condensates oscillate in-phase, the particle streams emitted from the two condensates interfere constructively in the open channel of the Y-coupling, which maximizes the overall losses of the coupled condensate system. Destructive interference, and thus a minimization of losses, occurs with condensates in antiphase configuration. In this way, the Y-coupling potential leads to a splitting in the imaginary components of the complex energies of the two states. An example of a condensate system coupled in this way is shown in Fig. 1e. The density distribution indicates an overall antisymmetric wavefunction that describes two condensates in antiphase configuration. An important difference between the direct and the Y-coupling method is that the direct coupler a priori does not favor in-phase or antiphase correlations, while the Y-coupling investigated in this work only creates antiphase correlations. If, for example, the arm lengths in the coupling potentials were varied (keeping the overall mirror symmetry of the system), a change in sign of the phase correlations is expected in the case of the direct coupling but not for the Y-coupling (see also the Supplementary Note 2). In the latter case, in-phase correlations can only be expected if the mirror symmetry of the coupling potential is broken.

It is important to emphasize that, strictly speaking, neither the direct coupling method described above is purely dispersive nor the Y-coupling is purely dissipative. Direct particle exchange leads to a splitting of the frequencies of in-phase or antiphase
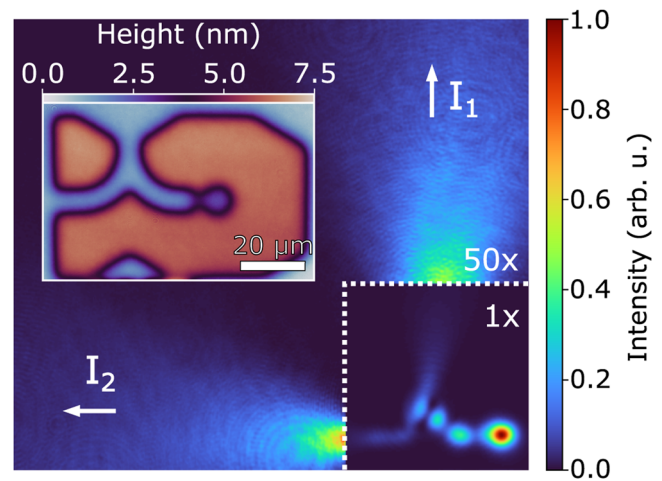

Fig. 2 Flow of light in the Y-coupler. A modified Y-coupler structure, as shown in the top left inset figure, is used to determine the splitting between photons flowing out of the structure at the exits (I_1, I_2). I_1 contributes to the dissipative component of the coupling, while I_2 contributes a dispersive component. The measured photon density in the area marked with '50x' is multiplied by that factor in order to improve visibility of this low intensity region and highlight the spatial extent of the wavefunction. The measured intensity is averaged over 100 pulses.

coupled condensates. The frequency-dependent absorption governed by the Kennard-Stepanov law then contributes a dissipative component in the case of the direct coupling potential. For the Y-coupling potential, the particle flow that is emitted by one condensate is not fully directed into the open end of the coupling, but rather partially reaches the other condensate, which makes the coupling partially dispersive. To quantify this effect, we can measure the splitting ratio introduced by the Y-coupling potential, see Fig. 2. To do that, the potential is modified by removing one of the condensate confining potentials and replacing it by a second open end. This allows for the determination of the splitting ratio by integrating all light leaving the structure towards either exit and comparing the intensities. We find that $(62 \pm 5)\%$ of the particle flow emitted by one condensate leaves the Y-coupling potential through the designated loss channel, while $(38 \pm 5)\%$ of the particles would reach the other condensate. This light contributes a dispersive component to the coupling which, however, does not prevent the overall dissipative behavior of the coupling (see Supplementary Note 2).

Critical coupling. An important parameter for spin-glass simulation is the strength of the coupling. The coupling strength dictates the timescale of the synchronization process of the condensate phases. In principle, stronger coupling translates into faster computation times. Stronger coupling can also counteract inhomogeneities in the natural (uncoupled) condensate frequencies caused, for example, by manufacturing imperfections leading to a more robust simulation. The latter is suggested, for example, by the well-known Kuramoto model, which predicts a synchronization process if the coupling strength exceeds a critical value that depends on the natural frequency bandwidth of the oscillators[45].

To demonstrate and quantify critical coupling in systems of coupled photon BECs, we systematically increase the detuning of the natural condensate frequencies and determine the degree of synchronization. In order to achieve a controlled detuning of the condensate frequencies, we tilt one of the mirrors of the microresonator using piezoelectric actuators. Based on eq. (1),
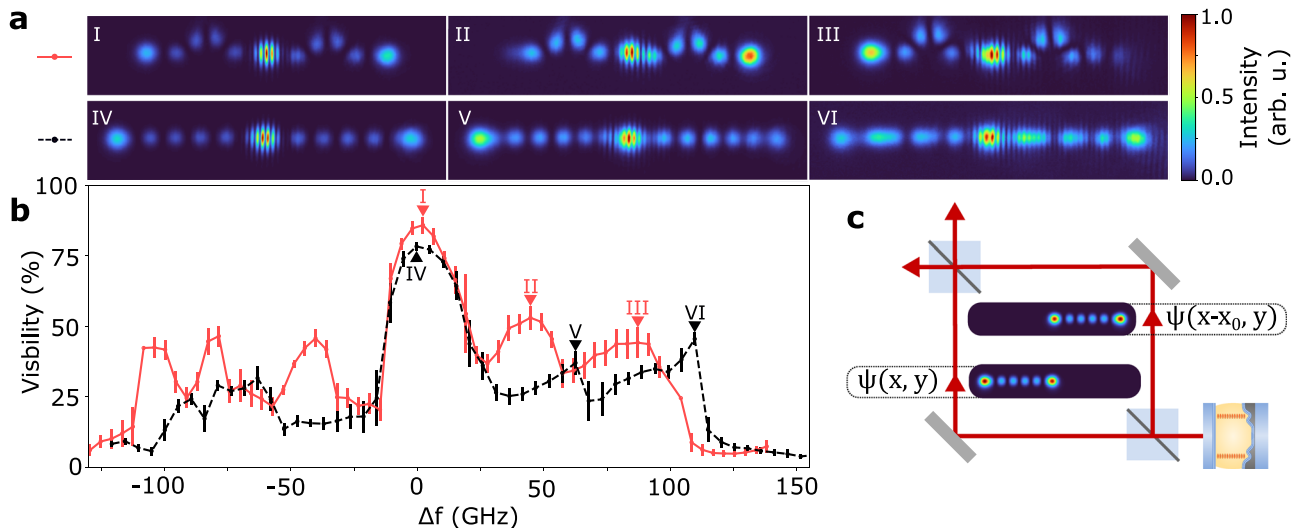
Fig. 3 Determination of the critical coupling. To determine the critical coupling, we record the fringe visibility of the interference between the two condensates as function of detuning in the natural frequencies. **a** Images of the interference between the coupled condensates as a function of detuning. To achieve an accurate estimate of the interferometric visibility, we take the mean of the central 5 fringes and average that over 100 pulses. Given error bars correspond to one standard deviation from the mean. **b** Interferometric visibility as a function of detuning between individual condensates. The Y-coupler (red solid line) and direct coupler (black dashed line) both show several breakdowns and revivals of the visibility. Data points I–III mark the maxima of these revivals for the Y-coupler and correspond to the labeled images. The same holds for data points IV–VI and the direct-coupler curve. **c** Schematic representation of the Mach-Zehnder interferometer used for superposing the condensates and creating the interference pattern.

tilting the cavity mirrors with respect to each other creates a potential gradient. This gradient results in a potential difference between the condensate sites and thus in a detuning between the natural frequencies of the condensates. The experimental quantification of this detuning is by no means trivial. In order to realize this experimentally, we use a potential reconstruction method that we introduced in an earlier work[18]. Further details are given in Supplementary Note 1. The determination of the degree of synchronization, on the other hand, can be realized quite naturally by means of an interferometric measurement. The light transmitted through the cavity mirrors is passed through a balanced Mach-Zehnder interferometer before it is detected on a camera. The interferometer is intentionally misaligned such that the two condensate wavefunctions overlap and interfere on the camera creating a stripe pattern. The interferometric visibility of this pattern is taken as a direct measure for the coherence between the two condensates.

In Fig. 3 we show experimental results that describe the coherence of two coupled BECs as a function of detuning of their natural frequencies. The results suggest that the phase coupling of the condensates can withstand a detuning of up to 100 GHz until it is finally lost and the condensates start to oscillate independently. It turns out, however, that the coherence for both the direct coupling potential and the Y-coupling potential is lost in a non-monotonic way, i.e., several breakdowns and revivals in the visibility of the condensate interference can be observed. The experimentally obtained mode patterns suggest that this non-monotonic behaviour could be related to changes between in-phase and antiphase correlations with increasing detuning, i.e., sign changes in the first-order correlations $g^{(1)}$ of the two condensates. Indeed, a linear potential gradient is expected to change the phase delay that the photons collect as they propagate in the region between the condensates, which could be the cause for such sign changes. However, this interpretation cannot be conclusively confirmed on the basis of our experimental data alone. This is mainly due to the fact that our experiments, as they are currently being carried out, only determine the visibility of the interference, i.e., $|g^{(1)}|$, but do not reveal the sign in the first-order

correlations. To investigate this situation further, we carried out numerical simulations that allow us to access the underlying $g^{(1)}$-function. Further details are given in Supplementary Note 2. The results of these simulations indeed support the above interpretation that the breakdowns and revivals of the visibility are caused by sign changes in $g^{(1)}$.

The visibility in Fig. 3 is shown as function of both positive and negative detunings. In principle, one would expect that the graphs should be fully symmetric with respect to zero detuning - which is, however, not the case. This results from the axis of rotation being offset compared to the center of the structure. In this way, a common frequency offset is introduced for both condensates, which is not reflected in the value of the detuning, but which can be different for positive and negative detunings and thus breaks the symmetry of the measurement curve to some extent.

Time-resolved synchronization process. In a second set of experiments, we investigate the condensation and synchronization process in a time-resolved manner using a streak camera. As before, we let the light from the cavity pass through an interferometer in order to make the coherence of the two coupled condensates visible as an interference pattern. This interference pattern is imaged onto the entrance slit of a streak camera so that we can examine it in a time-resolved manner after exciting the cavity with a nanosecond optical pulse. An example of such a measurement is shown in Fig. 4a. Here, the light intensity is shown along a cross section through the interference pattern as a function of time. In the case shown, two interference fringes are visible (located within a few micrometer around $x = 0$), which can be analyzed to determine the fringe visibility. Figure 4b, c show the average normalized intensity and fringe visibility as a function of time (when averaging over several hundred excitation pulses). From these measurements it can be concluded that the time evolution of the condensate population is rather similar for the two types of coupling (red and black curves). Differences arise, however, in the time evolution of the visibility. Here, our measurements show that the coherence is established somewhat faster with the direct coupling (rise time (440 ± 10) ps) than with
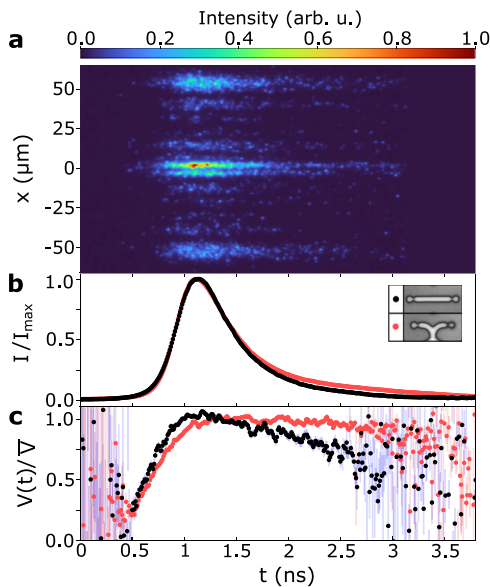
Fig. 4 Time-resolved coherence and condensate population for the direct and Y-coupler. a Streak camera image of a condensation process in the Y-coupler. This is a time-resolved measurement of the photon density along the cross section of the coupler. The central spot contains interference between both condensates, the visibility of these fringes over time is measured as $V(t)$. Due to (shot) noise in the measurement, averaging over many pulses is required. We postselect the pulses to remove formation jitter and intensity fluctuations. This leaves 247 and 757 out of 4000 images for the direct coupler and Y-coupler, respectively. **b** Averaged intensity envelopes of the direct coupler (black) and the Y-coupler (red), normalized to the maximum intensity. Both curves are very similar in envelope, the slightly longer tail in the pulse of the Y-coupler most likely stems from pump pulse fluctuations present in a subset of all streak camera images. **c** Fringe visibility of the interference between the two condensates for the direct coupler (black) and Y-coupler (red), visibility is normalized to the time-averaged visibility of the integrated pulse. Error bars show the standard error for all data points.

the Y-coupling (rise time $(570 \pm 10)\,\text{ps}$). On the other hand, almost full coherence is retained with the Y-coupling even when the condensate population drops again, while the coherence in the direct coupling potential decreases more quickly.

In general, spin-glass simulation based on networks of photon or polariton BECs not only requires precise control of the physical couplings between the condensates, it is also necessary to control the condensate populations, since these represent scaling factors for the effective coupling in the simulated XY model[9,18]. To create a homogeneous network of condensates that all have the same population, it can generally be necessary to distribute the optical gain inhomogeneously over the network. A natural question that arises is how the two types of coupling examined in this work behave with regard to inhomogeneous or unbalanced optical pumping. In contrast to the experiments carried out so far, we will concentrate the optical gain to a single condensate location in the following measurements to answer this question.

Figure 5 shows two examples for the time evolution of the condensate populations in the case of direct coupling (Fig. 5a, b) and Y-coupling (Fig. 5c, d). Although only one condensate location at $x = 30\,\mu\text{m}$ experiences optical gain in these experiments, a second condensate at $x = -30\,\mu\text{m}$ forms for both coupling types, the population of which is fed solely through particle exchange with the other condensate. In the case of direct coupling (Fig. 5c), this even goes so far that both condensate populations are almost identical (population ratio 1.17). Although
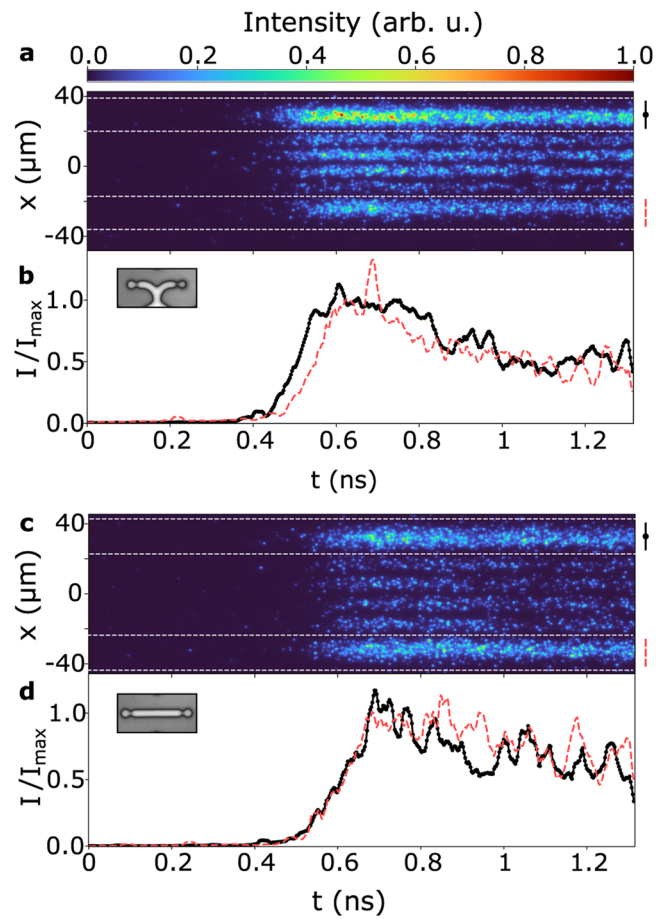

Fig. 5 Time delay in condensation under imbalanced optical pumping. a Streak camera image of the Y-coupler condensate under single-site illumination. **b** The spatially integrated intensity of the streak camera image regions marked by the white-dashed lines, where the condensates are located. The black line corresponds to the optically pumped condensate. A clear delay in intensity build up is apparent in both figures. Both intensities are normalized to the average of the 50 maximum values. **c, d** The same measurement, as in (**a**, **b**) for a condensation in the direct coupler structure. For the determination of the delay and populations imbalance, the values are ensemble averaged over 38 pulses for the direct coupler and 99 pulses for the Y-coupler. The reason for the difference in pulse numbers is the necessity of postselection due to the formation jitter.

this behavior may seem counterintuitive at first, an equal population of the condensates is indeed theoretically expected if the coupling rate between the condensates is sufficiently high[18]. In case of the Y-coupling potential (Fig. 5a), the direct particle exchange is deliberately suppressed, so that, as expected, significantly different condensate populations result (population ratio 2.78). Further differences between the two types of coupling arise in the temporal dynamics of the condensation process. To investigate this, we determine the normalized condensate population I/I_{max} for both condensates, see Fig. 5b, d. While both condensates are formed almost synchronously for the case of direct coupling (time delay of $(9 \pm 2)\,\text{ps}$), the formation of the second condensate has a considerable time delay of $(36 \pm 2)\,\text{ps}$ in case of the Y-coupling potential.

A substantially different dynamical behavior than shown in Fig. 5 is observed when the system is set in a parameter range between two stable configurations. The latter can be achieved, for example, by introducing a small mismatch between the location of the optical pumping and the confining potential of the
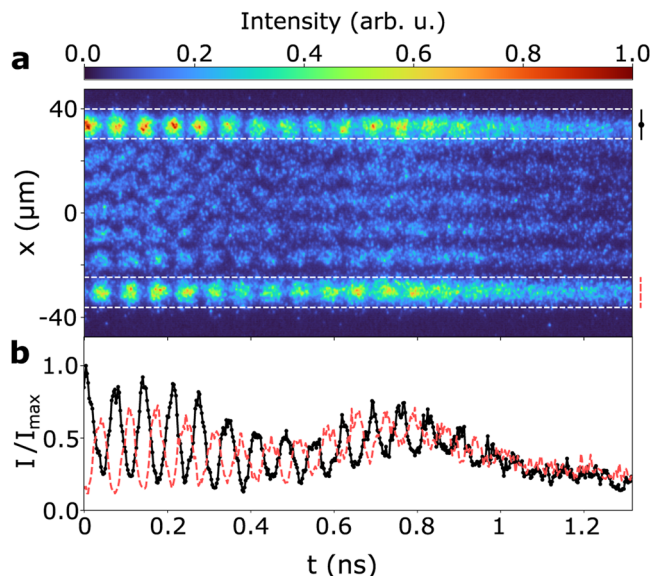
Fig. 6 Coherent oscillation under imbalanced optical pumping of the direct coupler. a Streak camera image of the direct coupler with off-center pumping of a single condensate (compared to the confining potential). **b** Integrated intensity of the individual condensate sites. An oscillation is present with a frequency of (14.5 ± 0.5) GHz resulting from the coherent superposition of the antisymmetric state (with 6 nodes) and the symmetric state (with 5 nodes). The oscillation is damped as the system evolves from a superposition of both states into the single lower-energy antisymmetric state.

condensate, as is done in the measurement shown in Fig. 6. In this case, we observe that the system tends to go through oscillations in the condensate populations. These oscillations are caused by superposition states that arise when two (or more) different states experience similar optical gain and thus both are realized simultaneously by the system[33]. In the example of Fig. 6, this is a superposition of a symmetric wavefunction with 6 nodes and an antisymmetric wavefunction with 5 nodes. The observed oscillation frequency of 14.5 ± 0.5 GHz can be considered as the difference between the real parts of the complex energies of these two states. Interestingly, it turns out that this superposition state is not stable. For longer periods of time, the antisymmetric state starts to dominate, so that the oscillations in the condensate populations eventually disappear. It seems plausible to consider this as part of a thermalization process in which the state with the lower energy prevails due to the lower reabsorption by the optical medium. A similar phenomenon was previously observed in harmonically trapped photon gases[39]. We would like to emphasize that the oscillative behavior shown in Fig. 6 is quite typical for the direct coupling of two condensates. In particular, it also occurs in the case of symmetrical optical pumping. Both the experimentally determined photon densities and our numerical simulations suggest that superposition states and oscillative behavior occur at the breakdowns of visibility in the tilting experiment in Fig. 3.

Discussion

In this work we investigated the dynamics of a two-condensate system with dissipative and dispersive couplings. One of the most interesting applications of such a system is to use it as a building block for an analog spin-glass simulator. At this point, various physical platforms for realizing such simulators are being explored. All approaches face several challenges, such as replacing

conventional digital electronic components in the computing process, miniaturization, all-to-all coupling, and scaling. For the coupled photon BEC system, scaling to larger system sizes seems to be the most difficult challenge. The larger the network of photon BECs, the larger is the bandwidth of the natural (uncoupled) condensate frequencies, since even the best resonator mirrors are not perfectly flat. In principle, this can lead to phase coherence only being established for subsystems, but not for the system as a whole. The good news, however, is that the coupling of the condensates is relatively strong and thus also quite robust against detuning caused by mirror imperfections. From Fig. 3 it can be seen, for example, that a detuning of 10 GHz in the natural frequencies only leads to a minor decrease in coherence in the coupled system. Converted into a height difference, a detuning of 10 GHz corresponds to a height difference of 0.2 nm (assuming a resonator length of $10\,\mu m$). This means that the mirrors used should not have any height deviations greater than 0.2 nm in an area of, for example, several square millimeters in order to sufficiently restrict the bandwidth of natural frequencies in the BEC network. This is at the limit of what is technically feasible today, but it seems achievable. The direct-laser-writing technique we use for nanostructuring mirror surfaces does indeed achieve this level of accuracy. It is furthermore possible to actively control the condensate frequencies using a thermo-responsive optical medium[40].

Mapping a spin model Hamiltonian to the gain function of an optical spin-glass simulator is a prerequisite for the simulator to start sampling low-energy configurations. It is furthermore desirable that the dynamics of the simulator have fixed points (including the ground state of the simulated spin model). In the photon BEC system and related platforms this is only the case if the dispersive part of the physical couplings is sufficiently small[9]. Dissipative types of coupling, as proposed and investigated in this work, are particularly desirable in this regard. Another requirement is the ability to control the condensate populations individually. Here, interesting differences arise between the two types of coupling investigated in this work. As shown in Fig. 5, direct coupling tends to balance the populations of coupled condensates even with unbalanced optical gain. This property can be useful in specific cases, for example, for simulations of spin models on N-regular graphs[18]. In general, however, one would like the condensate population to be precisely controllable by the provided optical gain, which is indeed possible with the Y-coupling, since it keeps direct particle exchange sufficiently low. For the future, it seems both possible and desirable to combine dispersive and dissipative types of coupling by controlling the flow of photons between the condensates, for example, with the help of refractive index changes[18]. This would extend the class of physical models that can be investigated using analog simulations.

Methods

Microcavity system. The microcavity is formed from two high-finesse mirrors, one of which is nano-structured using a direct-laser-writing method, see Ref. [44]. The height profiles of the mirror surfaces are determined via Mirau interferometry. We use a commercially available interferometric microscope objective for this purpose (20X Nikon CF IC Epi Plan DI). The large free spectral range of the cavity, combined with the limited gain bandwidth of the dye, causes the longitudinal mode number to be a conserved quantity under repeated absorption and emission cycles. We work at mirror separations between $D \simeq 5\,\mu m$ and $D \simeq 10\,\mu m$ for the time-averaged measurements and $D \simeq 30\,\mu m$ for time-resolved measurements. The benefits of working at these comparatively large mirror separations are increased signal strength and reduced sensitivity to surface imperfections.

Optical medium. The dye in the microcavity consists of 10 mmol/l rhodamine 6G dissolved in ethylene glycol. We use an optical parametric oscillator with a 5 ns pulse duration at 490 nm to optically excite the dye.

Time-resolved measurements. For the time-resolved measurements, we use the streak camera Hamamatsu C10910-01 with a M10913-01 slow single sweep unit.

Further experimental and theoretical methods are presented in Supplementary Notes 1 and 2.

Data availability

Code availability

The code for the numerical simulations in our work is available upon request from the corresponding author.

References

1. Nixon, M., Ronen, E., Friesem, A. A. & Davidson, N. Observing geometric frustration with thousands of coupled lasers. *Phys. Rev. Lett.* **110**, 184102 (2013).
2. Marandi, A., Wang, Z., Takata, K., Byer, R. L. & Yamamoto, Y. Network of time-multiplexed optical parametric oscillators as a coherent Ising machine. *Nat. Photonics* **8**, 937–942 (2014).
3. McMahon, P. L. et al. A fully programmable 100-spin coherent Ising machine with all-to-all connections. *Science* **354**, 614–617 (2016).
4. Inagaki, T. et al. Large-scale Ising spin network based on degenerate optical parametric oscillators. *Nat. Photonics* **10**, 415–419 (2016).
5. Inagaki, T. et al. A coherent Ising machine for 2000-node optimization problems. *Science* **354**, 603–606 (2016).
6. Ohadi, H. et al. Nontrivial phase coupling in polariton multiplets. *Phys. Rev. X* **6**, 031032 (2016).
7. Berloff, N. G. et al. Realizing the classical XY Hamiltonian in polariton simulators. *Nat. Mater.* **16**, 1120–1126 (2017).
8. Lagoudakis, P. G. & Berloff, N. G. A polariton graph simulator. *N. J. Phys.* **19**, 125008 (2017).
9. Kalinin, K. P. & Berloff, N. G. Global optimization of spin Hamiltonians with gain-dissipative systems. *Sci. Rep.* **8**, 1–9 (2018).
10. Ohadi, H. et al. Synchronization crossover of polariton condensates in weakly disordered lattices. *Phys. Rev. B* **97**, 195109 (2018).
11. Kalinin, K. P. & Berloff, N. G. Polaritonic network as a paradigm for dynamics of coupled oscillators. *Phys. Rev. B* **100**, 245306 (2019).
12. Pal, V., Mahler, S., Tradonsky, C., Friesem, A. A. & Davidson, N. Rapid fair sampling of the XY spin Hamiltonian with a laser simulator. *Phys. Rev. Res.* **2**, 033008 (2020).
13. Parto, M., Hayenga, W. E., Marandi, A., Christodoulides, D. N. & Khajavikhan, M. Nanolaser-based emulators of spin Hamiltonians. *Nanophotonics* **9**, 4193–4198 (2020).
14. Parto, M., Hayenga, W., Marandi, A., Christodoulides, D. N. & Khajavikhan, M. Realizing spin Hamiltonians in nanoscale active photonic lattices. *Nat. Mater.* **19**, 725–731 (2020).
15. Alyatkin, S., Töpfer, J., Askitopoulos, A., Sigurdsson, H. & Lagoudakis, P. Optical control of couplings in polariton condensate lattices. *Phys. Rev. Lett.* **124**, 207402 (2020).
16. Kalinin, K. P., Amo, A., Bloch, J. & Berloff, N. G. Polaritonic XY-Ising machine. *Nanophotonics* **9**, 4127–4138 (2020).
17. Kalinin, K. P. & Berloff, N. G. Toward arbitrary control of lattice interactions in nonequilibrium condensates. *Adv. Quantum Technol.* **3**, 1900065 (2020).
18. Vretenar, M., Kassenberg, B., Bissesar, S., Toebes, C. & Klaers, J. Controllable Josephson junction for photon Bose-Einstein condensates. *Phys. Rev. Res.* **3**, 023167 (2021).
19. Onsager, L. A two-dimensional model with an order-disorder transition. *Phys. Rev.* **65**, 117 (1944).
20. Berezinskii, V. L. Destruction of long-range order in one-dimensional and two-dimensional systems possessing a continuous symmetry group. ii. quantum systems. *Sov. Phys. JETP* **34**, 610–616 (1972).
21. Kosterlitz, J. M. & Thouless, D. J. Ordering, metastability and phase transitions in two-dimensional systems. *J. Phys. C: Solid State Phys.* **6**, 1181 (1973).
22. Barahona, F. On the computational complexity of Ising spin glass models. *J. Phys. A: Math. Gen.* **15**, 3241 (1982).
23. Cubitt, T. & Montanaro, A. Complexity classification of local Hamiltonian problems. *SIAM J. Comput.* **45**, 268–316 (2016).
24. Lucas, A. Ising formulations of many NP problems. *Front. Phys.* **2**, 5 (2014).
25. Johnson, M. W. et al. Quantum annealing with manufactured spins. *Nature* **473**, 194–198 (2011).
26. Boixo, S. et al. Evidence for quantum annealing with more than one hundred qubits. *Nat. Phys.* **10**, 218–224 (2014).
27. King, A. D. et al. Observation of topological phenomena in a programmable lattice of 1,800 qubits. *Nature* **560**, 456–460 (2018).
28. Honari-Latifpour, M. & Miri, M.-A. Mapping the x y Hamiltonian onto a network of coupled lasers. *Phys. Rev. Res.* **2**, 043335 (2020).
29. Honari-Latifpour, M. & Miri, M.-A. Optical Potts machine through networks of three-photon down-conversion oscillators. *Nanophotonics* **9**, 4199–4205 (2020).
30. Struck, J. et al. Engineering Ising-XY spin-models in a triangular lattice using tunable artificial gauge fields. *Nat. Phys.* **9**, 738–743 (2013).
31. Aleiner, I. L., Altshuler, B. L. & Rubo, Y. G. Radiative coupling and weak lasing of exciton-polariton condensates. *Phys. Rev. B* **85**, 121301 (2012).
32. Kalinin, K. P. & Berloff, N. G. Simulating Ising and n-state planar Potts models and external fields with nonequilibrium condensates. *Phys. Rev. Lett.* **121**, 235302 (2018).
33. Ding, J., Belykh, I., Marandi, A. & Miri, M.-A. Dispersive versus dissipative coupling for frequency synchronization in lasers. *Phys. Rev. Appl.* **12**, 054039 (2019).
34. Ding, J. & Miri, M.-A. Mode discrimination in dissipatively coupled laser arrays. *Opt. Lett.* **44**, 5021–5024 (2019).
35. Klaers, J., Schmitt, J., Vewinger, F. & Weitz, M. Bose-Einstein condensation of photons in an optical microcavity. *Nature* **468**, 545–548 (2010).
36. Klaers, J., Vewinger, F. & Weitz, M. Thermalization of a two-dimensional photonic gas in a 'white wall'photon box. *Nat. Phys.* **6**, 512–515 (2010).
37. Klaers, J., Schmitt, J., Damm, T., Vewinger, F. & Weitz, M. Statistical physics of Bose-Einstein-condensed light in a dye microcavity. *Phys. Rev. Lett.* **108**, 160403 (2012).
38. Kirton, P. & Keeling, J. Nonequilibrium model of photon condensation. *Phys. Rev. Lett.* **111**, 100404 (2013).
39. Schmitt, J. et al. Thermalization kinetics of light: From laser dynamics to equilibrium condensation of photons. *Phys. Rev. A* **92**, 011602 (2015).
40. Dung, D. et al. Variable potentials for thermalized light and coupled condensates. *Nat. Photonics* **11**, 565–569 (2017).
41. Walker, B. T. et al. Driven-dissipative non-equilibrium Bose-Einstein condensation of less than ten photons. *Nat. Phys.* **14**, 1173–1177 (2018).
42. Greveling, S., Perrier, K. L. & van Oosten, D. Density distribution of a Bose-Einstein condensate of photons in a dye-filled microcavity. *Phys. Rev. A* **98**, 013810 (2018).
43. Gladilin, V. N. & Wouters, M. Classical field model for arrays of photon condensates. *Phys. Rev. A* **101**, 043814 (2020).
44. Kurtscheid, C. et al. Realizing arbitrary trapping potentials for light via direct laser writing of mirror surface profiles. *EPL (Europhys. Lett.)* **130**, 54001 (2020).
45. Acebrón, J. A., Bonilla, L. L., Vicente, C. J. P., Ritort, F. & Spigler, R. The Kuramoto model: a simple paradigm for synchronization phenomena. *Rev. Mod. Phys.* **77**, 137 (2005).

Acknowledgements

Author contributions

C.T. and M.V. performed the experimental studies. All authors carried out the analysis. J.K. performed the theoretical modeling and supervised the work.

Competing interests

The authors declare no competing interests.

Additional information

Supplementary information The online version contains supplementary material available at https://doi.org/10.1038/s42005-022-00832-3.

Correspondence and requests for materials should be addressed to Jan Klaers.

Peer review information *Communications Physics* thanks Hamid Ohadi and the other, anonymous, reviewer(s) for their contribution to the peer review of this work. Peer reviewer reports are available.

Reprints and permission information is available at http://www.nature.com/reprints

Publisher's note Springer Nature remains neutral with regard to jurisdictional claims in published maps and institutional affiliations.